

RESEARCH ARTICLE | JANUARY 14 2025

## Low voltage and high bandwidth surface-illuminated three-terminal Ge-on-Si APD with multiple biasing configurations



Huan Qu ; Xuetong Li ; Xiaobin Liu; Weipeng Wang; Yingzhi Li; Baisong Chen; Heming Hu ; Zihao Zhi ; Ziming Wang ; Jie Li ; Guoqiang Lo ; Lei Wang ; Quanxin Na ; Xueyan Li ; Xiaolong Hu ; Qijie Xie ; Junfeng Song



*Appl. Phys. Lett.* 126, 021105 (2025)

<https://doi.org/10.1063/5.0239942>



View  
Online



Export  
Citation

### Articles You May Be Interested In

Time-lens-based optical phased array LiDAR for ranging and accuracy enhancement

*APL Photonics* (November 2025)

On-chip infrared photonics with Si-Ge-heterostructures: What is next?

*APL Photonics* (May 2022)

$\text{Ge}_{0.95}\text{Sn}_{0.05}$  on Si avalanche photodiode with spectral response cutoff at  $2.14 \mu\text{m}$

*APL Photonics* (October 2025)

**°BLUE FORS**

**More wiring. More qubits. More results.**  
The world's most popular fridge just got better.

[Discover the new side-loading LD system](#)

# Low voltage and high bandwidth surface-illuminated three-terminal Ge-on-Si APD with multiple biasing configurations

Cite as: Appl. Phys. Lett. **126**, 021105 (2025); doi: [10.1063/5.0239942](https://doi.org/10.1063/5.0239942)

Submitted: 29 September 2024 · Accepted: 20 December 2024 ·

Published Online: 14 January 2025



[View Online](#)



[Export Citation](#)



[CrossMark](#)

Huan Qu,<sup>1</sup> Xuetong Li,<sup>1</sup> Xiaobin Liu,<sup>1</sup> Weipeng Wang,<sup>1</sup> Yingzhi Li,<sup>1</sup> Baisong Chen,<sup>1</sup> Heming Hu,<sup>1</sup> Zihao Zhi,<sup>1</sup> Ziming Wang,<sup>1</sup> Jie Li,<sup>1</sup> Guoqiang Lo,<sup>2</sup> Lei Wang,<sup>3</sup> Quanxin Na,<sup>3</sup> Xueyan Li,<sup>1</sup> Xiaolong Hu,<sup>1</sup> Qijie Xie,<sup>3,a)</sup> and Junfeng Song<sup>1,3,a)</sup>

## AFFILIATIONS

<sup>1</sup>State Key Laboratory of Integrated Optoelectronics, College of Electronic Science and Engineering, Jilin University, Changchun 130012, China

<sup>2</sup>Advance Micro Foundry, Pte Ltd, 11 Science Park Road, Science Park II, Singapore 117685, Singapore

<sup>3</sup>Peng Cheng Laboratory, Shenzhen 518000, China

<sup>a)</sup>Authors to whom correspondence should be addressed: [xiejq@pcl.ac.cn](mailto:xiejq@pcl.ac.cn) and [songjf@jlu.edu.cn](mailto:songjf@jlu.edu.cn)

## ABSTRACT

In this work, a regulated-voltage biasing configuration is proposed for the Ge-on-Si avalanche photodiode (APD) structure. This design incorporates an extended n-charge layer to decrease the breakdown voltage and optimizes the absorption region thickness to reduce the electron transit time. By applying three electrodes to individually modulate the electric fields in the absorption and avalanche region, respectively, both of low avalanche breakdown voltage ( $-8.1$  V) and high bandwidth (20.4 GHz) of the surface-illuminated detector can be achieved. Meanwhile, the sensitivity of weak light detection is improved to  $-45$  dBm. The responsivity of the APD is  $60.76$  A/W at 1550 nm when the voltage is biased at  $-13.5$  V. The low voltage and improved bandwidth can meet the requirements for weak light detection and other applications demanding such sensitivity.

Published under an exclusive license by AIP Publishing. <https://doi.org/10.1063/5.0239942>

Avalanche photodiode (APDs) are important optoelectronic devices<sup>1–5</sup> with a wide range of applications in consumer and military fields. Compared with waveguide structures,<sup>6–8</sup> surface-illuminating APDs can efficiently collect scattered optical signals in free-space communication<sup>9,10</sup> and are therefore suitable for applications in autonomous driving and LiDAR.<sup>11</sup> Complementary-metal-oxide semiconductor (CMOS)-compatible Ge-on-Si APDs can be integrated with other optoelectronic devices on the same substrate to form integrated optoelectronic circuits, making them suitable for mass production.<sup>12</sup> Ge has strong absorption properties up to 1550 nm due to its small bandgap. Since the 1550 nm wavelength is safe for the human eye, it has a high potential for use in LiDAR systems. Three-terminal APDs allow separate electrical control of the absorption and multiplication processes by using three electrodes with two independent voltages onto the absorption and multiplication regions simultaneously. Therefore, an external reverse bias voltage can be directly applied on three-terminal APDs without affecting carrier extraction in the absorption region, enabling lower avalanche voltage than that of conventional

separated-absorption-charge-multiplication (SACM) APDs.<sup>13</sup> In the LiDAR system, a boost circuit can be used to power our APD. This places higher demands on Ge-on-Si APDs with low breakdown voltage and large bandwidth in order to realize low-cost, high-performance APDs.<sup>14,15</sup>

In this paper, a Ge-on-Si n-type charge layer doped avalanche photodiode (APD) structure is meticulously designed through the multiple biasing configuration of device. This design aims to maintain high optical absorption efficiency while reducing the thickness and area of the absorption region to minimize junction capacitance and decrease carrier transit time. Additionally, by optimizing the doping concentration of the charge layer, the breakdown voltage is effectively lowered, thereby achieving more precise control over the electric field.

Notably, this design employs multiple biasing configurations applied to P-Ge and P-Si, respectively. This approach effectively modulates the electric field distribution between the absorption and multiplication layers, enhancing the internal electric field intensity, accelerating carrier drift velocity, and thus optimizing the

photodetector's bandwidth performance. This innovative scheme presents a approach to achieving higher bandwidth on the Ge-on-Si platform.

The study demonstrates the current characteristics and radio frequency (RF) response properties of a three-electrode Ge-on-Si APD. TCAD simulation software was utilized to model the electric fields and carrier velocities within the device. Similar to traditional (SACM) APD<sup>16,17</sup> models, an equivalent circuit model incorporating parasitic effects for the active region of the APD was simulated to elucidate the enhancement in the RC-limited bandwidth. Based on simulation results, the device was fabricated, tested, and analyzed. Compared with our previous work,<sup>18,19</sup> this is the demonstration that applying bias voltages to a three-terminal surface-illuminated Ge-on-Si APD with an extended n-type charge layer can achieve low voltage high bandwidth performance.

The devices were fabricated on silicon-on-insulator (SOI) wafers with 220 nm of top silicon using a standard process at advanced micro foundry (AMF), Singapore. Ge was grown by selective silicon and germane epitaxial growth using the reduced pressure CVD (RPCVD) process. The device structure is shown in Fig. 1(a); after the device is completed, all APDs are covered with silica dioxide. The specific preparation steps for the device are as follows. The top silicon layer is etched to define the silicon grid pattern. Boron and phosphorus are implanted on the wafer to form p-type and n-type regions, respectively. The Si p++ and Si n++ regions are the two terminals of the silicon. A Ge layer was then epitaxially grown on the lightly doped

n-type region. The dimensions of the epitaxial Ge are 15  $\mu\text{m}$  (length)  $\times$  15  $\mu\text{m}$  (width)  $\times$  500 nm (height). The Ge film is grown intrinsically and is subsequently implanted on the top surface to form Ge p++, which creates the Ge termination contact. The Ge-on-Si APD device schematic is shown in Fig. 1(b), which consists of a Ge absorption region on the left and a Si APD on the right that is connected by a Si n+ bridge.

By optimizing the doping concentration of the charge layer, an increased doping level effectively reduces the breakdown voltage, thereby enabling more precise control of the electric field. Through theoretical TCAD modeling, the electric field distribution under multiple biasing configurations was characterized. The electric field profile of the Ge-on-Si APD device was simulated under bias voltages applied to the Si p++ terminal. Figures 1(c) and 1(d) show the electric field in the Si layer in the position from A to A1 and B to B1, respectively. When 1550 nm infrared light is normally incident on the surface of Ge-on-Si APD, the photogenerated carriers in the Ge absorption region are swept through the electric field into the high-field Si i-multiplication region where avalanche multiplication occurs. The inset shows a simulation of the electric field in the Ge region, where the electric field is obtained by applying  $-25\text{ V}$  to the Si p++ terminal, while Si n++ and Ge are at ground potential. The results show that the electric field in the absorber layer of the Ge layer is  $1.3 \times 10^4 \text{ V/cm}$  ( $> 10^4 \text{ V/cm}$ ),<sup>20</sup> which ensures that the carriers move in the absorber layer at a saturated drift velocity. Meanwhile, the structure has an electric field of  $2.1 \times 10^5 \text{ V/cm}$  in the Si avalanche region at a bias voltage of  $-28\text{ V}$ , which is larger than the threshold electric field in Si that triggers avalanche multiplication.

In another configuration, Figs. 1(e) and 1(f) illustrate the electric field distributions along the vertical direction from point C to C1 and along the horizontal direction from point A to A1, respectively, under varying bias voltages ranging from 0 to  $-15\text{ V}$  applied to the Ge terminal. These simulations reveal that the electric field strength within the germanium absorption region can be maintained above  $10^5 \text{ V/cm}$ , which is necessary to achieve impact ionization. The unique biasing configuration of the APD structure facilitates both light absorption and carrier multiplication within the germanium region, leading to an optimized electric field distribution. The elevated electric field within the Ge region facilitates efficient carrier generation and multiplication. Consequently, this design approach substantially enhances the performance and sensitivity of the Ge-on-Si APD device.

The DC characteristics of the three-electrode were simulated for comparison with the experimental results, by applying reverse bias at the Ge terminal. When the voltage is increased to a certain level, the dark current and photocurrent of the device rise sharply, and then, the device is in the avalanche state, which is capable of weak light detection. The voltage value with the dark current of the device reaching  $10^{-5} \text{ A}$  is defined as the avalanche breakdown voltage,<sup>21</sup> and the avalanche breakdown voltage of the device is  $-8.1\text{ V}$ .

The I-V characteristics and responsivity were characterized using the Santec TSL-510 laser as the light source. Light was illuminated directly above the Ge active layer of the detectors through single mode fiber. Meanwhile, the probes contacted the APD's electrode pads, which are connected to the Keysight B1500A for data reading. The responsivity was calculated by dividing the photocurrent by the input optical power.

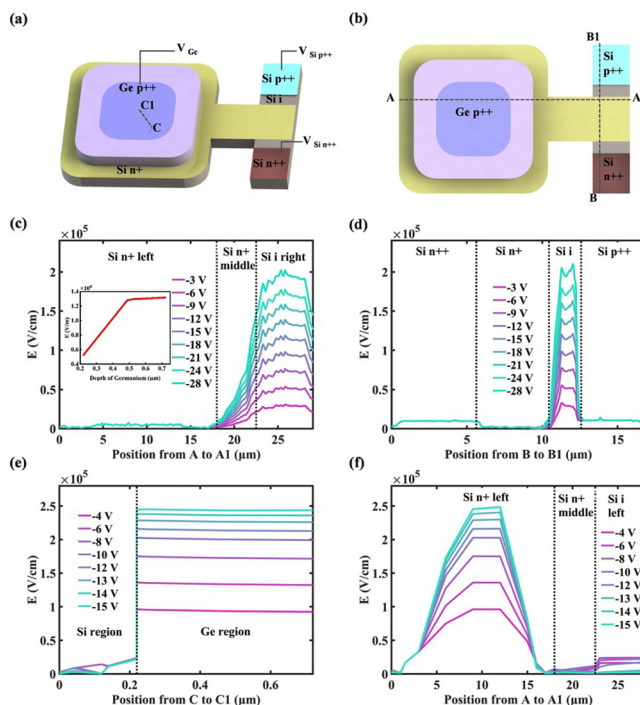


**FIG. 1.** (a) Structural and (b) schematic diagram of Ge-on-Si APD; (c) x and (d) y direction electric field simulation in the Si region with different bias voltages applied at the Si p++ terminal; inset (c) shows the simulated electric field in the Ge region; (e) z direction electric field simulation in the Ge region; and (f) x direction electric field simulation in the Si region with different voltage applied at the Ge terminal.

To better understand the device operating detail of the three-terminal APD and analyze the practical weak light detection capability of the device, the Si p++ terminal was at ground, the Ge terminal scanning voltage was -11 V, and different fixed voltages were applied to the Si n++ electrode ( $V_{Si\ n^{++}}$ ). The effects of different fixed voltages  $V_{Si\ n^{++}}$  on the dark current and photocurrent are shown in Figs. 2(a) and 2(b). As  $V_{Si\ n^{++}}$  increases, both the dark current and the photocurrent gradually increase, reaching the avalanche voltage and resulting in avalanche multiplication. The avalanche multiplication gain<sup>22</sup> is calculated from the ratio of the responsivity R at the bias voltage ( $V_{bias}$ ) to the main responsivity  $R_0$  at the voltage with unit gain. The dark current level at the voltage corresponding to unit gain is approximately  $10^{-7}$  A. Hence, the corresponding photocurrent and the responsivity curves can be obtained. As illustrated in Figs. 2(c) and 2(d), when  $V_{Si\ n^{++}}$  varies from 0 V to 6 V, the responsivity is 0.3 A/W, with a corresponding gain of 1.2. Compared to the previously proposed responsivity<sup>19</sup> of 0.08 A/W, the responsivity has increased by a factor of three. This improvement enables the photodetector to more capable of detecting weak signals and enhance its sensitivity.

The DC characteristic curves for the two configurations responding to different input optical power at 1550 nm have been measured. The first configuration, defined as the P-Si biasing configuration, involves scanning the Si p++ terminal of the three-electrode while setting 0 V on the Si n++ and Ge p++ terminals. Figures 3(a) and 3(b) show the photocurrent and responsivity of the first configuration. The avalanche breakdown voltage is -24.9 V, and the responsivities for optical powers of -10, -20, -30, and -40 dBm are 0.4, 1.47, 8.27, and 51.28 A/W, respectively. The second configuration, defined as the P-Ge biasing configuration, involves scanning the Ge p++ terminal of the three-electrode while setting 0 V on the Si p++ and Si n++ terminals. Figures 3(c) and 3(d) show the photocurrent and responsivity of the second configuration. The avalanche breakdown voltage is -8.1 V, and the responsivities for optical powers of -10, -20, -30, and -40 dBm are 0.56, 0.91, 3.05, and 7.08 A/W, respectively. Figures 3(e) and 3(f) show the gain curves of the APD for the first and second

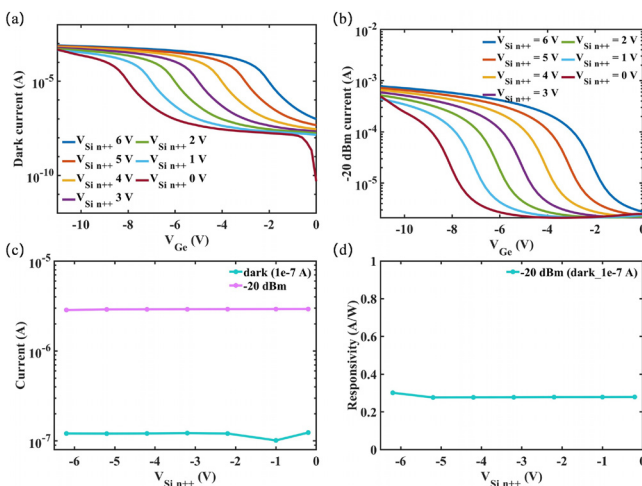


**FIG. 2.** (a) Dark current; (b) photocurrent at 1550 nm under input optical power -20 dBm; (c) current diagram, and (d) responsivity diagram for a dark current level at  $10^{-7}$  A of Ge terminal.

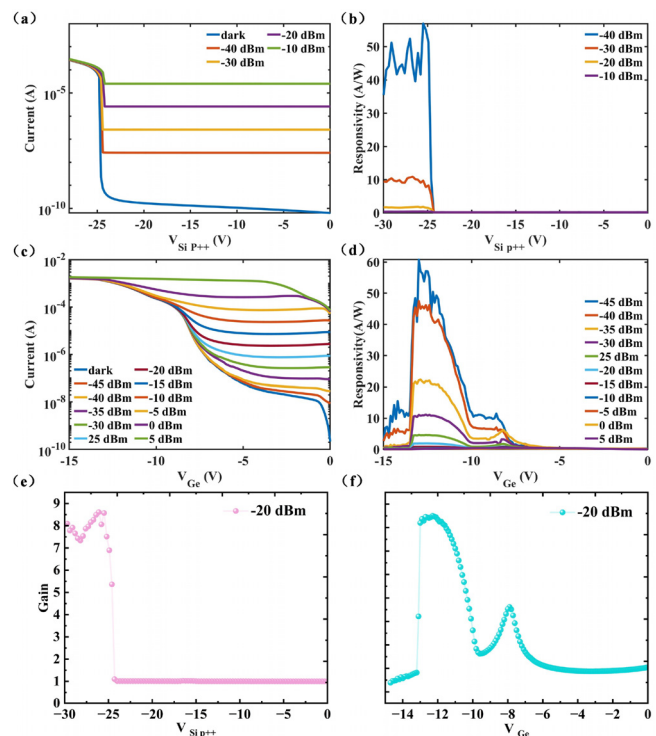


**FIG. 3.** (a) Current characteristic diagram and (b) responsivity characteristic diagram with P-Si biasing configuration; (c) current characteristic diagram and (d) responsivity characteristic diagram with P-Ge biasing configuration; and the tested gain at optical power -20 dBm with (e) P-Si and (f) P-Ge biasing configuration.

configurations, respectively, when the input optical power is -20 dBm. The measurement results show that when the bias voltage reaches -13.5 V, the avalanche multiplication effect increases due to the space charge effect, resulting in a further increase in both the photocurrent and the dark current. The weak light detection limit of the device is at least -45 dBm, and at this optical power, the maximum response can reach 60.76 A/W. A comparative analysis of the DC characteristics of the device was conducted based on the observed data, revealing that multiple biasing configurations significantly impact the dark current and breakdown voltage properties. The first biasing configuration results in a dark current at an extremely low level, reaching the pA level, with a higher avalanche breakdown voltage. Conversely, the second biasing configuration demonstrates a lower breakdown voltage, which is particularly advantageous for subsequent circuit design and implementation, providing enhanced suitability for circuit integration due to its lower avalanche breakdown voltage.

To characterize the high-speed performance of the device, the bandwidth of the APD was measured at different voltages. The Light-wave Component Analyzer (LCA, Keysight, N5222B) is used to measure the S21 curve of the APD. Figure 4(f) shows flow charts of the experimental setup for measuring the surface-illuminated Ge-on-Si APD bandwidth.

Figure 4(a) shows the 1550 nm frequency response of the APD measured at different bias voltages. Here, the optical power is set to  $P_{in} = -20$  dBm, and the APD has a 3-dB bandwidth of 0.27 GHz

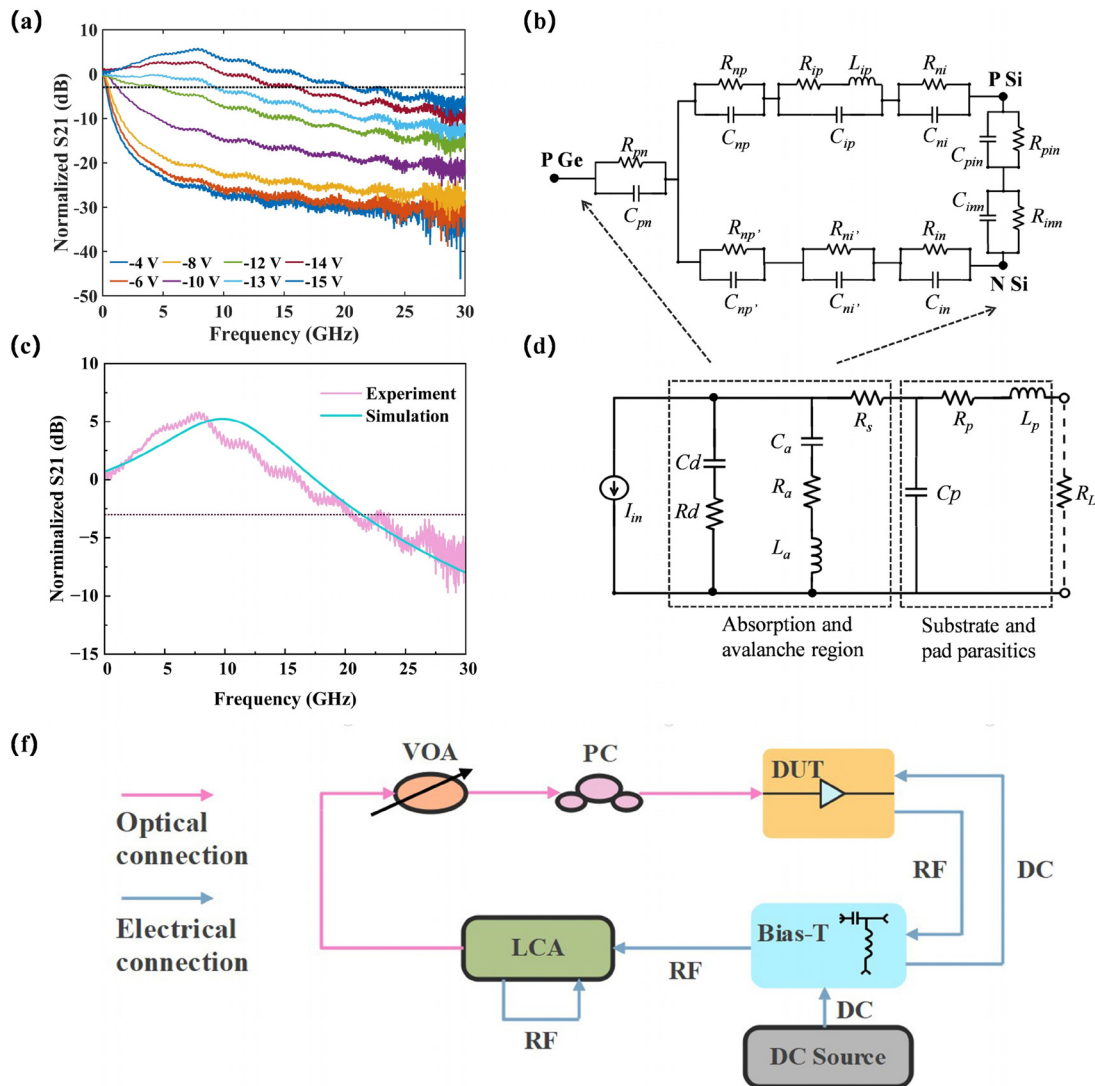


**FIG. 4.** (a) The 1550 nm frequency response measured at different bias voltages of the Ge terminal; (b) electric model of the Ge-on-Si APD; (c) measured and simulated electrical output impedances at  $-15\text{ V}$  reverse bias; (d) simplified circuit model of a three-terminal APD; (f) experimental setup of bandwidth test. (LCA, light wave component analyzer; VOA, variable optical attenuator; PC, polarization controller; RF, radio frequency; and DC, direct current.)

when operating at a bias voltage of  $V_{\text{bias}} = -4\text{ V}$ . The 3-dB bandwidth is limited due to incomplete depletion of the germanium region. It can be seen that the bandwidth further increases above  $1.14\text{ GHz}$  with a gain higher than 3.5, as shown in Fig. 3(f), when  $|V_{\text{bias}}| > 10.5\text{ V}$ . This is attributed to the space charge effect generated by the high current density, which has been observed in previous studies.<sup>6,17,23</sup> The space charge effect may introduce behavior similar to the inductance peak, which helps to increase the bandwidth of the APD.<sup>6</sup> When  $|V_{\text{bias}}|$  is increased to  $13\text{ V}$ , both gain and bandwidth increase. When  $|V_{\text{bias}}| = 13\text{ V}$ , the bandwidth is  $9.29\text{ GHz}$ , and the gain is 7.46 [as shown in Fig. 3(f)]. When the bias voltage,  $|V_{\text{bias}}|$ , is further increased to  $15\text{ V}$ , it produces a high bandwidth,  $20.4\text{ GHz}$ , but the gain-bandwidth product (GBP) decreases slightly due to the lower gain. At

a lower input optical power, a higher GBP can be achieved due to the higher gain.

The theoretical calculation of the bandwidth provides insight into and facilitates the analysis of the high-speed performance of the devices. It is known that the 3-dB bandwidth of a photodetector is primarily dominated by the carrier transit time-limited bandwidth  $f_{\tau}$  and RC-limited bandwidth  $f_{RC}$  in the active region. The carrier transit time-limited bandwidth  $f_{\tau}$  can be written as<sup>24</sup>

$$f_{\tau} = \frac{0.45v}{d}, \quad (1)$$

where  $v$  is the saturation drift velocity and  $d$  is the thickness of the intrinsic layer. The RC-limited bandwidth  $f_{RC}$  can be written as

**TABLE I.** Fitted electric circuit parameters of a three terminal APD.

Parameters	$R_a(\Omega)$	$C_a(fF)$	$L_a(nH)$
Values	6000	60	1000
Parameters	$R_p(\Omega)$	$C_p(fF)$	$L_p(nH)$
Values	25	4	9
Parameters	$R_d(\Omega)$	$C_d(fF)$	$R_s(\Omega)$
Values	950	7	25

$$f_{RC} = \frac{1}{2\pi RC}, \quad (2)$$

where  $R$  is the resistance, which consists of the series resistance and the load resistance, and  $C$  is the capacitance, including the junction capacitance and the parasitic capacitance. The 3-dB bandwidth can be estimated by Ref. 25

$$f_{3-\text{dB}} = \frac{1}{\sqrt{f_\tau^{-2} + f_{RC}^{-2}}}. \quad (3)$$

The RC circuits are simulated to analyze the factors contributing to the large bandwidth. Figure 4(b) shows an equivalent electric model of the active regions of a three-terminal APD, excluding parasitic elements. Three electric terminals (P-Ge, P-Si, and N-Si) contact germanium, P-doped silicon, and N-doped silicon regions, respectively. In the comprehensive model illustrated in Fig. 4(b), a pair of lumped capacitor and resistor in parallel are used to model the current path between the three electric terminals and the boundary “p-n.” Additionally, a lumped inductance is employed to model the charge multiplication regions. This extra inductance originates from the space charge effect<sup>23</sup> due to the carrier buildup from charge avalanche multiplication. The circuit elements modeled in Fig. 4(b) can be fitted from

scattering parameter (S-parameter) measurements. The S-parameters between any two of the three electrical terminals were characterized consecutively. To measure all the photocurrent generated in the device, the P-doped silicon and N-doped silicon regions were shorted by wire bonding to simplify the current measurement with one GS probe. Figure 4(d) shows the electric circuit diagram where the P-doped silicon and N-doped silicon are shorted and circuit elements are grouped together. Specifically, the three-terminal APD electrical parasitic include those in the diode junctions and avalanche regions, as well as substrate and pad parasitic. Here,  $R_d$  is the resistance in the absorption region,  $R_a$  is the capacitance in the absorption region, and  $C_a$  is the capacitance in the avalanche region. The inductor  $L_a$ , together with its series resistance  $R_d$ , is due to space charge effects.  $R_s$  is the diode series resistance,  $C_p$  is the parasitic capacitance,  $R_p$  is the parasitic resistance, and  $L_p$  is the parasitic inductance. Values of these parameters were fitted, and example values at reverse bias of  $-15$  V are shown in Table I. The parameter S21 of the three terminal APD was then fitted parameter values of circuit components, and they matched very well with measured values, as presented in Fig. 4(c).

The higher performance of the APD devices presented here has been achieved mainly by redesigning the device doping profile and fabrication process to eliminate germanium impact ionization. Specifically, the doping of the charge layer was increased to better confine the electric field inside the silicon, and the avalanche breakdown voltage was substantially lowered. Another noteworthy aspect is the optimization of the thickness and area of the absorption region, which reduces the junction capacitance (including the  $C_a$  and  $C_d$ ) in the photodetector.

In addition to simulating the equivalent circuit, the carrier velocities in different directions also were simulated with TCAD modeling. Figures 5(a) and 5(b) show distributions of electron velocity in the XZ plane and XY plane. Figures 5(c) and 5(d) show the simulated carrier velocity of the APD operating at different bias voltages on Ge terminal

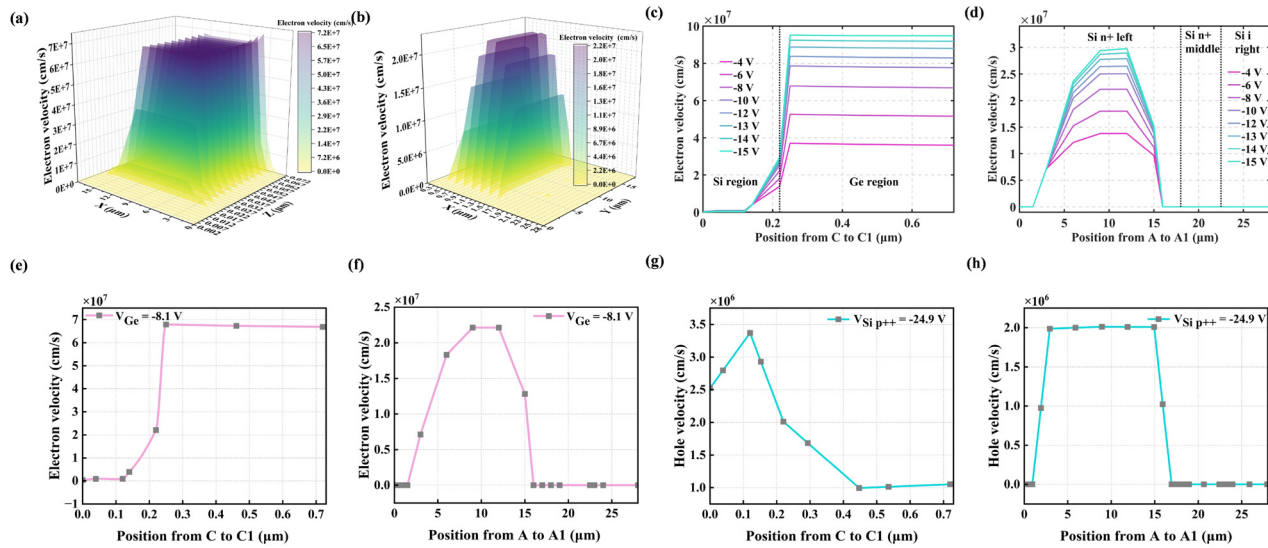


**FIG. 5.** Distribution of simulated electron velocity in (a) XZ and (b) XY plane; electron velocity curve position from (c) C to C1 and (d) A to A1 with different bias voltages applied at the Ge terminal; electron velocity curve position from (e) C to C1 and (f) A to A1 with  $-8.1$  V bias voltages applied at the Ge terminal; and hole velocity curve from position C to C1 (g) and (h) A to A1 with  $-24.9$  V bias voltages applied at the Si p++ terminal.

**TABLE II.** Device performance of surface-illuminated APDs.

References	Wavelength (nm)	Breakdown voltage (V)	Dark current (A)	Responsivity (A/W)	3-dB BW (GHz)
1	1310	-25	$10^{-6}$	5.88	11.5
9	1550	-27	$10^{-4}$	12.7	/
18	1550	-25	$10^{-7}$	1.17	0.043
19	1550	-56	$10^{-7}$	9.97	0.142
20	1550	-13.3	$10^{-7}$	0.243	0.001 53
22	1550	-9.8	$10^{-6}$	/	12
27	1550	-29.4	$3 \times 10^{-5}$	0.3	8
28	1550	-26.5	$7.8 \times 10^{-5}$	0.35	12
This work (P-Si biasing)	1550	-24.9	$10^{-5}$	51.28	11.8
This work (P-Ge biasing)	1550	-8.1	$10^{-5}$	7.08	20.4

along the tangent line where X is equal to 9 [position from C to C1 as shown in Fig. 1(a)] and where Y is equal to 11.5 [position from A to A1 as shown in Fig. 1(b)]. There is a positive correlation between the carrier velocities and the different bias voltages.

The bandwidth of the P-Si bias configuration is 11.8 GHz. To compare the carrier rates under p-Si and p-Ge biasing configurations, simulations of electron velocity were conducted by varying the P-Ge terminal voltage around its respective avalanche breakdown point, as shown in Figs. 5(e) and 5(f). Similarly, simulations of hole velocity were performed by adjusting the P-Si terminal voltage near its avalanche breakdown voltage, with the results presented in Figs. 5(g) and 5(h). The hole saturation drift velocity for silicon and the electron saturation drift velocity for germanium have been set to  $7 \times 10^6$  cm/s.<sup>26</sup> Overall, the velocity of electrons biasing at the P-Ge terminal is higher than the velocity of holes biasing at the P-Si terminal. Electrons at the P-Ge terminal biased configuration achieve the saturation drift velocity, whereas holes at the P-Si terminal biased travel at a velocity below the saturation drift velocity. In the P-Ge biasing configuration, the electron transmission pathway aligns with the high-speed region created by the electric field distribution. The higher electron saturation velocity in germanium allows carriers to transit longer distances in the same amount of time. The faster carrier velocity and greatly reduced carrier transit time in the P-Ge biasing configuration contribute to an increase in the 3-dB bandwidth.

A three-electrode Ge-on-Si APD that is compatible with the complementary-metal-oxide semiconductor (CMOS) process has been reported. The three-electrode APD was tested and analyzed, demonstrating its ability to regulate the performance under multiple biasing configurations. When a scanning voltage is applied to the P-Si terminal, the proposed device achieves a dark current of approximately  $10^{-10}$  A and a responsivity of 51.28 A/W at an optical power level of -40 dBm, under a breakdown voltage of -24.9 V. When a scanning voltage is applied to the P-Ge terminal, the device achieves a dark current of  $10^{-7}$  A, a low breakdown voltage of -8.1 V, and a responsivity of 60.76 A/W at an input laser power of -45 dBm under bias voltage of -13.5 V. Operating at the bias voltage of -15 V exhibits an optimal bandwidth of 20.4 GHz. As shown in Table II, the performance of the device is significantly superior to that of other surface-illuminated devices. These characteristics make the device suitable for applications in LiDAR, weak light imaging, optical communication, and related fields.

This work is supported by the National Key R&D Program of China (Grants No. 2022YFB2804504); the National Natural Science Foundation of China (Grant Nos. 62090054 and 61934003); the National Natural Science Foundation of China (No. 62105173); the National Natural Science Foundation of China (No. 62105174); the Major Scientific and Technological Program of Jilin Province (Grants No. 20210301014GX); the Jilin Provincial Development and Reform Commission Project (No. 2020C056); and the Program for Jilin University Science and Technology Innovative Research Team (No. JLUSTIRT, 2021TD-39).

## AUTHOR DECLARATIONS

### Conflict of Interest

The authors have no conflicts to disclose.

### Author Contributions

**Huan Qu:** Conceptualization (lead); Data curation (lead); Formal analysis (lead); Writing – original draft (lead); Writing – review & editing (lead). **Xuetong Li:** Investigation (supporting). **Xiaobin Liu:** Formal analysis (supporting); Investigation (supporting). **Weipeng Wang:** Investigation (supporting). **Yingzhi Li:** Methodology (supporting). **Baisong Chen:** Validation (supporting). **Heming Hu:** Investigation (supporting). **Zihao Zhi:** Investigation (supporting). **Ziming Wang:** Methodology (supporting). **Jie Li:** Methodology (supporting). **Guoqiang Lo:** Validation (supporting). **Lei Wang:** Resources (supporting). **Quanxin Na:** Resources (supporting). **Xueyan Li:** Supervision (supporting). **Xiaolong Hu:** Supervision (supporting). **Qijie Xie:** Methodology (equal); Resources (equal). **Junfeng Song:** Funding acquisition (equal); Project administration (equal); Writing – review & editing (equal).

## DATA AVAILABILITY

The data that support the findings of this study are available from the corresponding authors upon reasonable request.

## REFERENCES

- Y. Kang, H.-D. Liu, M. Morse, M. J. Paniccia, M. Zadka, S. Litski, G. Sarid, A. Pauchard, Y.-H. Kuo, H.-W. Chen, W. S. Zaoui, J. E. Bowers, A. Beling, D. McIntosh, X. Zheng, and J. Campbell, "Monolithic germanium/silicon

- avalanche photodiodes with 340 GHz gain-bandwidth product," *Nat. Photonics* **3**, 59–63 (2009).
- <sup>2</sup>D. Benedikovic, L. Virot, G. Aubin, J.-M. Hartmann, F. Amar, X. L. Roux, C. Alonso-Ramos, E. Cassan, D. Marris-Morini, F. Boeuf, J.-M. Fedeli, B. Szelag, and L. Vivien, "Silicon-Germanium avalanche receivers with fJ/bit energy consumption," *IEEE J. Sel. Top. Quantum Electron.* **28**, 1–8 (2022).
- <sup>3</sup>A. Palmieri, M. Calciati, M. Vallone, G. Ghione, A. Tibaldi, F. Bertazzi, and M. Goano, "Energy balance modeling of Ge-on-Si waveguide avalanche photodetectors," in *17th International Conference on Numerical Simulation of Optoelectronic Devices NUSODsanta* (IEEE, Barbara, CA, 2017), pp. 211–212.
- <sup>4</sup>S. Srinivasan, M. Berciano, P. D. Heyn, S. Lardenois, M. Pantouvaki, and J. V. Campenhoult, "27 GHz silicon-contacted waveguide-coupled Ge/Si avalanche photodiode," *J. Lightwave Technol.* **38**, 3044–3050 (2020).
- <sup>5</sup>J. Zhang, B.-P. Kuo, and S. Radic, "64 Gb/s PAM4 and 160 Gb/s 16QAM modulation reception using a low-voltage Si-Ge waveguide-integrated APD," *Opt. Express* **28**, 23266–23273 (2020).
- <sup>6</sup>Y. Yuan, Z. Huang, X. Zeng, D. Liang, W. Sorin, M. Fiorentino, and R. Beausoleil, "High responsivity Si-Ge waveguide avalanche photodiodes enhanced by loop reflector," *IEEE J. Sel. Top. Quantum Electron.* **28**, 1–8 (2022).
- <sup>7</sup>N. Martinez, C. Derose, R. Brock, A. Starbuck, A. Pomerene, A. Lentine, D. Trotter, and P. Davids, "High performance waveguide-coupled Ge-on-Si linear mode avalanche photodiodes," *Opt. Express* **24**, 19072–19081 (2016).
- <sup>8</sup>Z. Huang, C. Li, D. Liang, K. Yu, C. Santori, M. Fiorentino, W. Sorin, S. Palermo, and R. Beausoleil, "25 Gbps low-voltage waveguide Si-Ge avalanche photodiode," *Optica* **3**, 793–798 (2016).
- <sup>9</sup>C. L. Hsin and C. H. Chou, "Buffer-free Ge/Si by rapid melting growth technique for separate absorption and multiplication avalanche photodetectors," *IEEE Electron Device Lett.* **40**, 945–948 (2019).
- <sup>10</sup>P. Vines, K. Kuzmenko, J. Kirdoda, D. Dumas, M. Mirza, R. Millar, D. Paul, and G. Buller, "High performance planar germanium-on-silicon single-photon avalanche diode detectors," *Nat. Commun.* **10**, 1086 (2019).
- <sup>11</sup>D. Dumas, J. Kirdoda, R. Millar, P. Vines, K. Kuzmenko, G. Buller, and D. Paul, "High-efficiency Ge-on-Si spads for short-wave infrared," in *Conference on Optical Components and Materials XVI* (SPIE, San Francisco, CA, 2019), Vol. 10914, pp. 389–395.
- <sup>12</sup>A. Sammak, M. Aminian, L. Qi, W. de Boer, E. Charbon, and L. Nanver, "A CMOS compatible Ge-on-Si APD operating in proportional and Geiger modes at infrared wavelengths," in *IEEE International Electron Devices Meeting (IEDM)* (IEEE, Washington, DC, 2011), p. 8.5.1.
- <sup>13</sup>B. Wang, Z. Huang, X. Zeng, R. Wu, W. Sorin, D. Liang, and R. Beausoleil, "A compact model for Si-Ge avalanche photodiodes," in *15th IEEE International Conference on Group IV Photonics (GFP)* (IEEE, Cancun, Mexico, 2018), pp. 109–110.
- <sup>14</sup>K. V. Acoleyen, K. Komorowska, W. Bogaerts, and R. Baets, "One-dimensional off-chip beam steering and shaping using optical phased arrays on silicon-on-insulator," *J. Lightwave Technol.* **29**, 3500–3505 (2011).
- <sup>15</sup>D. Kwong, A. Hosseini, Y. Zhang, and R. Chen, "1 × 12 unequally spaced waveguide array for actively tuned optical phased array on a silicon nanomembrane," *Appl. Phys. Lett.* **99**, 51104 (2011).
- <sup>16</sup>D. Dai, H. Chen, J. Bowers, Y. Kang, M. Morse, and M. Paniccia, "Equivalent circuit model of a waveguide-type Ge/Si avalanche photodetector," *Phys. Status Solidi (c)* **7**, 2532–2535 (2010a).
- <sup>17</sup>Z. H. B. Wang, X. Zeng, W. Sorin, D. Liang, M. Fiorentino, and R. Beausoleil, "A compact model for Si-Ge avalanche photodiodes over a wide range of multiplication gain," *J. Lightwave Technol.* **37**, 3229–3235 (2019).
- <sup>18</sup>X. Liu, X. Li, Y. L. Z. Zhi, B. Chen, Q. Xie, X. L. Q. Na, P. Guo, F. Gao, G. Lo, B. Kang, and J. Song, "Three-electrode germanium-on-silicon avalanche photodiode array," *Opt. Lett.* **48**, 1846–1849 (2023).
- <sup>19</sup>X. Liu, X. Li, Y. Li, Z. Zhi, M. Tao, B. Chen, L. Zhang, P. Guo, G. Lo, X. Li, F. Gao, B. Kang, and J. Song, "Three-terminal germanium-on-silicon avalanche photodiode with extended p-charge layer for dark current reduction," *Photonics Res.* **10**, 1956–1963 (2022).
- <sup>20</sup>Y. Li, X. Liu, X. Li, S. Wang, H. Ye, L. Zhang, Y. Li, S. Sun, B. Chen, Y. Ma, P. Guo, F. Gao, X. Li, G. Lo, and J. Song, "Surface illuminated interdigitated Ge-on-Si photodetector with high responsivity," *Opt. Express* **29**, 16346–16361 (2021).
- <sup>21</sup>Y. Kang, M. Zadka, S. Litski, G. Sarid, M. Morse, M. J. Paniccia, Y.-H. Kuo et al., "Monolithic Ge/Si avalanche photodiode receiver for 10 Gb/s 1.3 m application," in *LEOS 2008-21st Annual Meeting of the IEEE Lasers and Electro-Optics Society* (IEEE, 2008), pp. 292–293.
- <sup>22</sup>Z. Huang, D. Liang, C. Santori, M. Fiorentino, C. Li, and R. G. Beausoleil, "Low-voltage Si-Ge avalanche photodiode," in *2015 IEEE 12th International Conference on Group IV Photonics (GFP)* (IEEE, 2015), pp. 41–42.
- <sup>23</sup>D. Dai, M. Rodwell, J. Bowers, Y. Kang, and M. Morse, "Derivation of the small signal response and equivalent circuit model for a separate absorption and multiplication layer avalanche photodetector," *IEEE J. Sel. Top. Quantum Electron.* **16**, 1328–1336 (2010b).
- <sup>24</sup>Z. Liu, F. Yang, W. Wu, H. Cong, J. Zheng, C. Li, C. Xue, B. Cheng, and Q. Wang, "48 GHz high-performance Ge-on-SOI photodetector with zero-bias 40 Gbps grown by selective epitaxial growth," *J. Lightwave Technol.* **35**, 5306–5310 (2017).
- <sup>25</sup>X. Li, Z. Liu, L. Peng, X. Liu, N. Wang, Y. Zhao, J. Zheng, Y. Zuo, C. Xue, and B. Cheng, "High-performance germanium waveguide photodetectors on silicon," *Chin. Phys. Lett.* **37**, 038503 (2020).
- <sup>26</sup>S. Huang, C. Li, Z. Zhou, C. Chen, Y. Zheng, W. Huang, H. Lai, and S. Chen, "Depth-dependent etch pit density in ge epilayer on si substrate with a self-patterned ge coalescence island template," *Thin Solid Films* **520**, 2307–2310 (2012).
- <sup>27</sup>N. Duan, T.-Y. Liow, A.-J. Lim, L. Ding, and G. Lo, "310 GHz gain-bandwidth product Ge/Si avalanche photodetector for 1550 nm light detection," *Opt. Express* **20**, 11031–11036 (2012).
- <sup>28</sup>G. Kim, S. Kim, S. Kim, J. Oh, and K.-S. Jang, "Ndr-effect vertical-illumination-type Ge-on-Si avalanche photodetector," *Opt. Lett.* **43**, 5583–5586 (2018).